Journal of
Biomedical Optics

BiomedicalOptics.SPIEDigitalLibrary.org

Shack–Hartmann-based objective straylight assessment of the human eye in an increased scattering angle range

Stefan Schramm
Patrick Schikowski
Elena Lerm
André Kaeding
Jens Haueisen
Daniel Baumgarten

SPIE.

Stefan Schramm, Patrick Schikowski, Elena Lerm, André Kaeding, Jens Haueisen, Daniel Baumgarten, "Shack–Hartmann-based objective straylight assessment of the human eye in an increased scattering angle range," *J. Biomed. Opt.* **21**(7), 076003 (2016), doi: 10.1117/1.JBO.21.7.076003.

Journal of Biomedical Optics 21(7), 076003 (July 2016)

Shack–Hartmann-based objective straylight assessment of the human eye in an increased scattering angle range

Stefan Schramm,[a,*] Patrick Schikowski,[b] Elena Lerm,[a] André Kaeding,[b] Jens Haueisen,[a] and Daniel Baumgarten[c]
[a]Technische Universität Ilmenau, Institute of Biomedical Engineering and Informatics, Department of Computer Science and Automation, Gustav-Kirchhoff-Straße 2, 98693 Ilmenau, Germany
[b]GMC Systems mbH, Albert-Einstein-Str. 3, 98693 Ilmenau, Germany
[c]University for Health Sciences, Medical Informatics and Technology, Institute of Electrical and Biomedical Engineering, Eduard Wallnöfer-Zentrum 1, Hall in Tirol 6060, Austria

Abstract. Objective measurement of straylight in the human eye with a Shack–Hartmann (SH) wavefront aberrometer is limited in imaging angle. We propose a measurement principle and a point spread function (PSF) reconstruction algorithm to overcome this limitation. In our optical setup, a variable stop replaces the stop conventionally used to suppress reflections and scatter in SH aberrometers. We record images with 21 diameters of the stop. From each SH image, the average intensity of the pupil is computed and normalized. The intensities represent integral values of the PSF. We reconstruct the PSF, which is the derivative of the intensities with respect to the visual angle. A modified Stiles Holladay approximation is fitted to the reconstructed PSF, resulting in a straylight parameter. A proof-of-principle study was carried out on eight healthy young volunteers. Scatter filters were positioned in front of the volunteers' eyes to simulate straylight. The straylight parameter was compared to the C-Quant measurements and the filter values. The PSF parameter shows strong correlation with the density of the filters and a linear relation to the C-Quant straylight parameter. Our measurement and reconstruction techniques allow for objective straylight analysis of visual angles up to 4 deg. [DOI: 10.1117/1.JBO.21.7.076003]

Keywords: ophthalmology; biomedical optics; straylight; glare; wavefront sensors; displays.

Paper 160050RR received Jan. 26, 2016; accepted for publication Jun. 8, 2016; published online Jul. 1, 2016.

1 Introduction/Motivation

The increase of scatter in the human eye lens is a common process during aging and cataractogenesis.[1–4] In consequence, glare increases and the image contrast reduces, whereas a loss of visual acuity due to straylight is hardly measurable. Typical diagnostic techniques for increased scatter can be categorized into indirect, subjective direct, and objective direct methods.

Indirect methods use the backscattered light from the lens to estimate the impairment of the forward scattered light on vision. This principle is used in slitlamps and Scheimpflug cameras. However, backscattered light is only weakly correlated with forward scattered light, particularly with regard to typical cataract development and increasing scatter particle size, which scatters more in the forward direction.[5]

Subjective direct methods for scatter measurement are realized with glare sensitivity tests, such as Mesotest II (Oculus GmbH, Wetzlar, Germany), and with the C-Quant straylight meter (Oculus GmbH, Wetzlar, Germany), which uses the compensation-comparison method.[6] With both tests, the straylight influence on the quality of functional vision could be assessed. It was shown that the individual straylight perception measured with the C-Quant has a high reproducibility.[7] In our previous work, we found in a group of 40 healthy subjects a Spearman–Roh correlation of $r = 0.514$ ($p < 0.001$) for straylight measured with the C-Quant and age.[8] Furthermore, the measurement time is long and the required interaction with the device might be cumbersome, particularly for older patients. Nevertheless, the C-Quant straylight meter gets increasing acceptance in visual science and clinical studies. It is also recommended for fitness-to-drive tests.[9]

The objective direct measurement methods of straylight are all based on double-pass techniques. Ginis et al. developed a scatter measurement device that enables the measurement of the point spread function (PSF) of the eye and therewith the straylight up to 8 deg by reconstructing a global PSF from different projections within a retinal image.[10,11] By using this approach, however, it is not possible to measure the straylight with local resolution in the pupil plane or in connection with aberrations.

Shack–Hartmann (SH) wavefront aberrometers also use the double-pass technique. In addition to the PSF position in every subaperture and subsequent wavefront reconstruction,[12] scatter metrics can be defined.[8,13–19] However, the subaperture images cover only angles of view of 1 to 2 deg. These angles are dominated by aberrations and are influenced by fundus scattering with respect to the reflection of the incoming laser beam, especially because of the use of infrared light in all common wavefront aberrometers, which penetrates deep into the fundus. This invalidates the central parts of the recording as proper scatter

---

*Address all correspondence to: Stefan Schramm, E-mail: stefan.schramm@tu-ilmenau.de

parameter.[20] Although previous studies showed correlations of some SH scatter metrics, they were very weak.[8]

We propose a measurement device based on an SH wavefront aberrometer. A variable stop enables the increase in the spatial extent of the PSF measurement. In combination with a newly developed analysis algorithm, it is possible to reconstruct the wide-angle PSF up to 4 deg. It enables the simultaneous spatially resolved imaging of scatter sources in the pupil plane and aberration measurement.

In this paper, the measurement device and the respective wide-angle PSF reconstruction algorithm are presented. For proof of principle, we performed a study with volunteers and compared the results with C-Quant measurements.

2 Methods

2.1 *Measurement Setup*

2.1.1 *Overview*

We used a variable stop. During the measurement, we increased the diameter of the stop stepwise. The mean intensity value for each SH subaperture changes continuously as a function of the stop diameter. The larger the stop diameter is, the larger the intensity is. If the subapertures start to overlap, the contributions from the neighboring subapertures start to add to the mean intensities. When the stop diameter reaches 2.8 deg visual angle, the peak intensities also start to increase with the increasing stop diameter. Roughly, the overlap of the subapertures produces part of the intensity, which is projected into the neighboring subapertures. At the same time, the neighboring subapertures project into the subaperture under consideration. Thus, in each subaperture, the mean intensity value will increase the same way it would without overlap and a larger visual angle. When averaging over all subapertures of the entire pupil, the effect of slightly different contributions of each subaperture to the neighboring ones vanishes. We obtained a function of mean intensity values over the stop diameter. This function is a representation of the integral function of the PSF of the eye. Consequently, we obtained the PSF of the eye by differentiation of this function with respect to the stop diameter.

Figure 1 shows an overview of the measurement device. Similar to a conventional SH wavefront aberrometer, the wavefront from the pupil plane is projected onto an SH sensor with a Kepler telescope (relay-system). We replaced the conventional field stop in an SH wavefront aberrometer with a digital mirror device (DMD). The DMD allows for arbitrary field stop geometries, in which variable circular stop geometries were used. Each of the images recorded by the SH sensor thus contains a different straylight contribution; the larger the stop diameter is, the larger the straylight contribution is. In the following Secs. 2.1.2–2.1.4, the parts of the measurement setups are explained in detail.

2.1.2 *Illumination*

A stabilized diode laser with a wavelength of 658 nm is employed for illumination. Shifting the incident laser beam parallel to the optical axis at the cornea by a scanning mirror, which is positioned in a conjugated plane to the retina, prevents the coupling of corneal reflections into the imaging path. However, in the case of ametropia, the illuminated point would move out of the fovea. Depending on the volunteer's refraction, measured with an autorefractor beforehand, the laser beam is focused by an optical trombone onto the retina. Thus, the laser spot is definitely positioned on the fovea, even in ametropic eyes.

As we used visible light, the volunteers fixated on the laser beam, which was a part of the instruction for each volunteer. This beam is relatively small, bright, and always sharply projected onto the retina, so that no accommodation impulse should be set.

2.1.3 *Imaging*

The imaging path contains two telescopes with a magnification between the pupil of the eye and the SH sensor of $M = 1$, respectively, realized by plano-convex lenses with a focal length of 75 mm (Fig. 1, L1 to L4). The first telescope system (L1 and L2) contains an optical trombone for focus correction. The value for correction was measured separately with an autorefractor prior to the actual experiment. A DMD was positioned in the intermediate image plane of the second telescope system (L3 and L4), enabling a maximum circular aperture of 10.5 mm in diameter.

The PSF of the eye is projected onto the DMD with a magnification of $M = 4.2$ (for the reduced Gullstrand model eye) with best spherical correction by varying the optical path length due to the refraction of the examined eye obtained before the measurement. This alignment is needed for the wavefront measurement and for the straylight measurement. Concerning correct wavefront measurement, the SH sensor has to work within its spatial dynamic range, so subaperture PSFs are not imaged under neighboring lenslets. With the setup of two telescopes and variation of the optical path length by an optical trombone, it is not necessary to move the DMD for focus correction. However, this setup requires an increased adjustment effort.

The SH sensor is built up with a Prosilica gc1380 camera (pixel size: $6.5 \times 6.5\ \mu$m; sensor size: 2/3”), a 10-mm × 10-mm microlens array with a lens pitch of 0.15 mm, a focal length of $f = 3.2$ mm, and thus has a magnification between the DMD and the subapertures of $M = 0.043$. The sensor is positioned in the focal plane of lens L4 under an angle of 24 deg to the optical axis of the incoming wavefront because of the peculiar reflection of the DMD. The microlens array is in parallel position to the camera sensor. Hence, the DMD plane is in focus only for the point of L4, which is on the optical axis of L4. However, the depth of field associated with the diameter of the microlenses and their focal length is large enough to image the complete DMD plane on the camera sharply.

These geometrical conditions lead to a distorted image of the pupil. A circular pupil is imaged as an ellipse. Concerning the wavefront measurement, this can be numerically corrected. However, this is not the focus of this paper. For the proposed scatter measurement, this has no effect.

Opposite to the SH sensor, a pupil camera is integrated. The camera is used for positioning the system in front of the volunteer's eye. The measurement system was moved in front of the volunteer's eye until the pupil was visible in the center of the pupil camera and the pupil border was sharply imaged. The system was calibrated with a plane reference wavefront. Calibration of the optical trombone was performed with spherical wavefronts of different radii. For this purpose, a single-mode

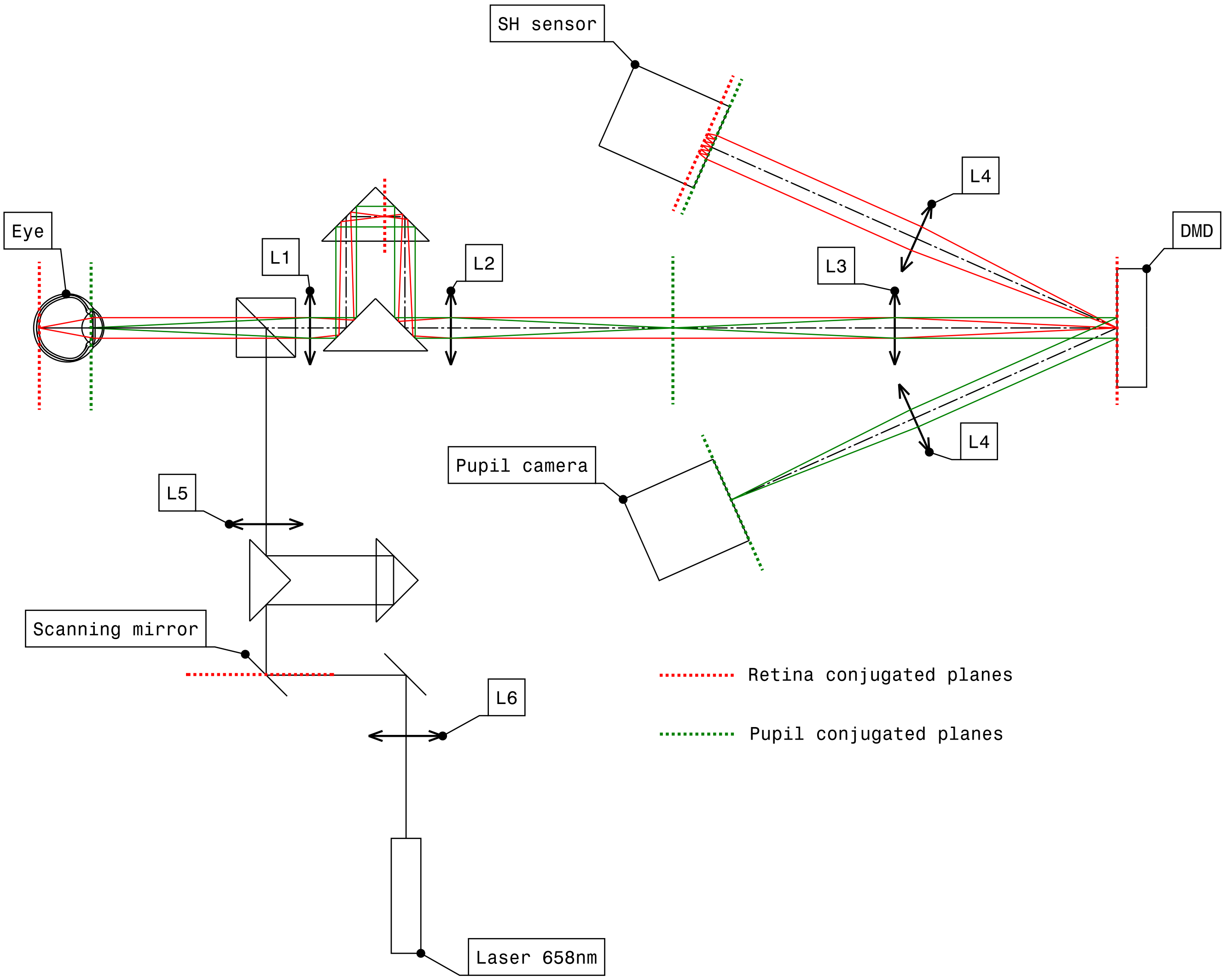

Fig. 1 Schematic measurement setup. The eye is illuminated by a diode laser of 658 nm with a parallel offset from the optical axis realized with a scanning mirror. The reflection is forming a wavefront, which is scattered and deformed at the anterior part of the eye. The deformed wavefront (red rays) and the scattered part (green rays) are separated by the stop geometry realized with the DMD. The deformed wavefront is projected onto the SH sensor. The scattered part is projected onto the pupil camera. Retina conjugated planes (red dotted lines) are in the optical trombone position, depending on the eye's refraction, on the DMD, and on the sensor plane of the SH sensor. Pupil conjugated planes (green dotted lines) are in the middle between the two telescope systems (between L2 and L3), on the pupil camera, and on the microlens plane of the SH sensor. In the illumination path, there is also a retina-conjugated plane at the center of rotation of the scanning mirror.

fiber-coupled diode laser was employed with the same wavelength as used for the illumination of the eye (658 nm).

2.1.4 *Digital mirror device*

The DMD (DMD 0.7 XGA 12 deg DDR DMD Discovery™, Texas Instruments) is a reflective display with an active area 14.008 mm wide and 10.506 mm high and composed of 1024×768 micromirrors that can be separately controlled. These micromirrors are tilting over their diagonal with a fixed angle of $+12$ and -12 deg.

DMDs were originally developed for the projector systems in which eventually distorted images, due to the peculiar reflection, could be digitally corrected. Here, the DMD is used within the imaging system. The main advantages over other display technologies are its high reflectivity of 89.4%, large fill factor of 88%, and low amount of scattering.

The DMD allows for the creation of different stop geometries and stop sequences. In our setup, the DMD is used for beam separation. While one part of the ray path, the wavefront (red rays in Fig. 1), is reflected onto the SH sensor, the inverse part of the stop geometry, the remains of the DMD area, is reflected onto the pupil camera (green ray in Fig. 1). We use a circular stop geometry around the PSF center in the intermediate image plane.

The DMD enables not only the use of different-shaped stop geometries but also the change of position of that stop in the intermediate image plane. The stop was positioned at the center of the PSF image before the measurement was started.

2.2 *Measurement Sequence*

During one measurement, the diameter of the stop is increased from $d = 0.5$ mm up to 10.5 mm in steps of 0.5 mm (21 images). This sequence is repeated five times for noise reduction. With every step, an SH image is captured and the average intensity of every subaperture is recorded.

The size of the image field (image of the PSF) in the DMD plane increases with increasing stop diameter. The image fields of every subaperture are increasing (Fig. 2). At an image angle of 1.4 deg on the fundus, the PSF images of the SH sensor [stop diameter at the DMD: 3.7 mm, Fig. 2(b)] start to overlap. With larger stop diameters, each PSF periphery overlaps the area of the adjacent PSFs. Consequently, information from the PSF periphery, which is dominated by scatter, is lost in common wavefront aberrometers. The reconstruction method described in Sec. 2.3 allows for extraction of information from the overlapping PSFs.

2.3 *Data Analysis*

The recorded SH images are analyzed in six steps: PSF detection and separation, pupil detection, subaperture image selection, subaperture image analysis, and parameter determination. These steps are performed on every SH image for every stop diameter. With the results from these calculations, the wide-angle PSF reconstruction is performed for one complete measurement sequence followed by statistical analysis of the study.

2.3.1 *Point spread function detection and separation*

In each SH image, all subaperture PSFs have to be detected and separated. The subaperture PSF detection in an SH image of the human eye with low contrast requires an increased algorithmic effort compared to common SH images in which typical threshold methods can be applied. We have implemented an algorithm, which detects the subaperture PSF centers in three steps. In a first step, all pixels in the image that belong to the histogram bins that exceed 99% of the cumulative histogram of the SH image over all subapertures are considered to be pixels near the center of the subapertures. (The 99% threshold was empirically determined.) The positions of those pixels are determined and in the second step, for each of these pixels, a radius of 10 pixels is searched for other pixels above the 99% criterion. The average position of all of these pixels is computed. This step yields a first approximation of each subaperture center due to the specific structure of the SH image. In the third step, the barycenters of the subaperture PSFs are determined by weighting the pixel coordinates with the intensities. This is done only for pixels within a radius of eight pixels around the first approximation of step two.

This procedure yields subpixel, accurate subaperture PSF positions that are used for further calculation. Rounded integer center coordinates are used to determine the subaperture tiles, where each tile is a square with an edge length of 21 pixels (maximum size of each lenslet). This step results in subaperture images for each lenslet for further analysis.

2.3.2 *Pupil detection*

The lenslet grid serves as the basis for the pupil detection in every SH image. On the lenslet grid, we define valid and invalid tiles. The valid tiles are the ones containing a subaperture PSF detected and separated in the previous step. The invalid tiles are the ones without such a detected subaperture PSF. An ellipse is fitted to the ensemble of valid tiles by using a genetic algorithm.[21,22]

The fit parameters are the x- and y-coordinates of the center point of the ellipse and the r_x and r_y half-axis lengths. The center point of the ensemble of valid tiles and the maximal extension of the valid tiles in x- and y-direction serve as initial guesses for the four fit parameters. The goal of the optimization is a fit of the ellipse such that a maximum number of valid tiles and a minimum number of invalid tiles are inside the ellipse.

2.3.3 *Subaperture image selection*

Not all subaperture PSFs are correctly imaged because eyelashes, reflections, and the pupil edge represent artifacts.

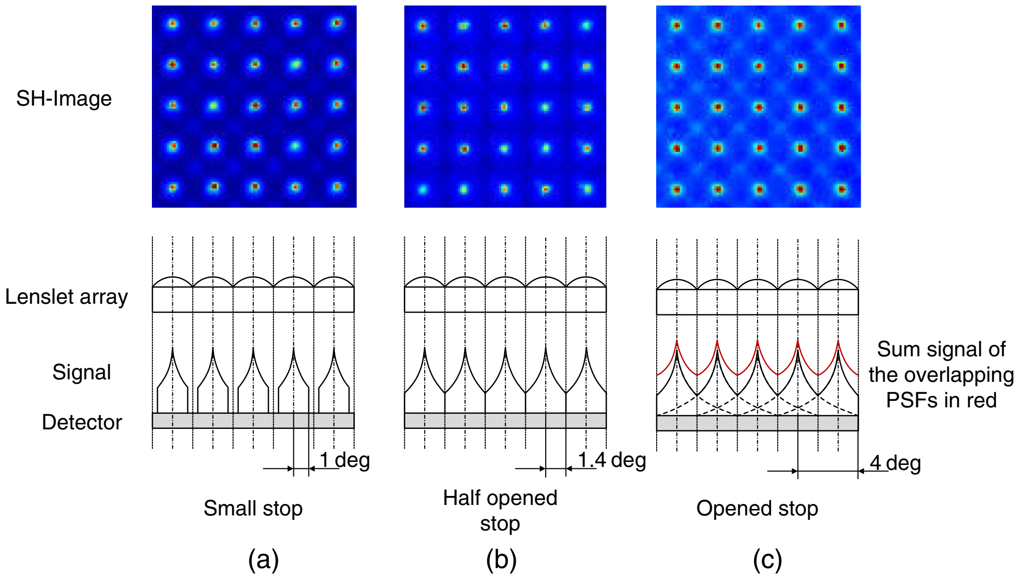

Fig. 2 Cross-sectional SH signal at different stop diameters. The opening of the stop is realized by the DMD [(a) stop diameter 2.5 mm; (b) stop diameter 3.7 mm; (c) stop diameter 10.5 mm].

Therefore, minimum quality criteria are defined. All subaperture PSFs outside the pupil are removed from the found set of subaperture images of each SH image. To eliminate boundary effects further, the outermost two layers of the subaperture images at the pupil border are also removed. From the remaining set, images with a mean intensity smaller than 2% of the mean intensity of all subaperture images are removed (low illumination due to eyelashes or other shadowing effects).

2.3.4 *Subaperture image analysis and parameter determination*

In the next step, statistical parameters are extracted from each subaperture image and subsequently averaged. Two subaperture-based straylight parameters are calculated: the cross-sectional area at half maximum (CAHM, Fig. 3), the number of pixels in the subaperture that have at least the half of the maximum intensity of the whole subaperture, and the moment (MOM) defined as the mean value of the intensity values $P(x,y)$, weighted with the squared distance R from the subaperture PSF center according to[14]

$$\mathrm{MOM} = \frac{\sum_{x,y} P(x,y) \cdot R_{x,y}^2}{\sum_{x,y} P(x,y)}. \tag{1}$$

Further, for the subsequent wide-angle PSF reconstruction (see below), the intensity of the subaperture PSFs is determined, and the mean intensity (I) over all selected subaperture images is computed (mean over all pixels and all selected subapertures).

2.3.5 *Wide-angle point spread function reconstruction*

The measured mean intensities I over all selected subapertures from the SH image sequence are the basis for the wide-angle PSF reconstruction.

In the following, we will use the spanned angle of vision θ as the main parameter describing the stop radius. Based on the system magnification, both can easily be converted into each other. The mean intensities I, which are computed for each stop diameter, can be expressed as a function of the angle of vision θ and represent an integral of the $\mathrm{PSF}_{\mathrm{eye}}$ following Eq. (2), assuming rotational symmetry of the $\mathrm{PSF}_{\mathrm{eye}}$

$$I(\theta) = \int_0^{\theta} 2\pi\nu \mathrm{PSF}_{\mathrm{eye}}(\nu)\mathrm{d}\nu. \tag{2}$$

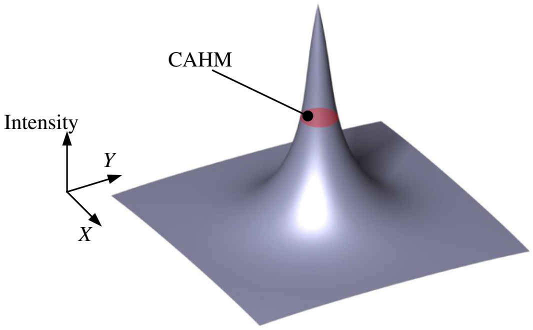

Fig. 3 Illustration of a PSF tile with the illustration of the parameter determination of the CAHM (red area).

Following the approach of Ginis et al.,[10] we fit a function to the measured mean intensities $I(\theta)$ to reduce the influence of noise. The least squares fitted mean intensity $I_{\mathrm{fit}}(\theta)$ is given as

$$I_{\mathrm{fit}}(\theta) = \frac{a \cdot \theta}{(\theta + b)^c}, \tag{3}$$

with a, b, and c being fit parameters. $I_{\mathrm{fit}}(\theta)$ is normalized to 1 at maximum stop size. The reconstructed PSF of the eye, $\mathrm{PSF}_{\mathrm{eye,rec}}$, can then be calculated by differentiation with respect to the visual angle

$$\mathrm{PSF}_{\mathrm{eye,rec}}(\theta) = \frac{1}{2\pi\theta}\frac{dI_{\mathrm{fit}}(\theta)}{d\theta}. \tag{4}$$

We approximate the $\mathrm{PSF}_{\mathrm{eye,rec}}$ with the finite differences method

$$\mathrm{PSF}_{\mathrm{eye,rec}}(\theta_i) \approx \frac{I_{\mathrm{fit}}(\theta_{i+1}) - I_{\mathrm{fit}}(\theta_i)}{A(\theta_{i+1}) - A(\theta_i)} \quad \text{with} \quad i = 1, \dots, 21, \tag{5}$$

where the 21 values of θ correspond to the 21 stop diameter values with the projected stop area A. The $\mathrm{PSF}_{\mathrm{eye,rec}}$ is energy corrected by a calibration factor, which includes system parameters such as camera response function, system transmission, and laser power. Scatter parameters within this resulting $\mathrm{PSF}_{\mathrm{eye,rec}}$ can be defined by fitting a generalized form of the Stiles Holladay approximation[23,24] to the $\mathrm{PSF}_{\mathrm{eye,rec}}$ with the scatter parameter S and the form parameter F

$$\mathrm{PSF}_{\mathrm{eye,fit}}(\theta) = \frac{S}{\theta^F}. \tag{6}$$

We define the straylight value IS according to van den Berg [Eq. (6)].[25] For better comparison with the C-Quant measurements, the logarithmic straylight value Log(IS) is calculated by using Eq. (8). The maximum visual angle in our setup is 4 deg. The straylight parameter $\mathrm{Log}(\mathrm{IS}_c)$ of the C-Quant is compared to our Log(IS) at this visual angle of 4 deg.

$$\mathrm{IS}(\theta) = \mathrm{PSF}_{\mathrm{eye,fit}}(\theta) \cdot \theta^2, \tag{7}$$

$$\mathrm{Log}[\mathrm{IS}(\theta)] = \mathrm{Log}\left(\frac{S}{\theta^F} \cdot \theta^2\right). \tag{8}$$

2.4 *Measurement Study*

For the proof of principle, we performed a measurement study with 16 eyes of 8 healthy volunteers in the age range of 24 to 31 years. The study was approved by the Ethics Committee of the Medical Faculty of the FSU Jena. All subjects gave written informed consent.

After the volunteer briefing and routine slit lamp examination, refraction and visual acuity were determined. Distance visual acuity (cc) was measured in logMAR units, using Landolt ring charts.

All volunteers underwent C-Quant measurements. Subsequently, scatter measurements with the device were performed in a darkened room after 10 min of dark adaptation. The total duration of the examination was about 1.5 h per volunteer.

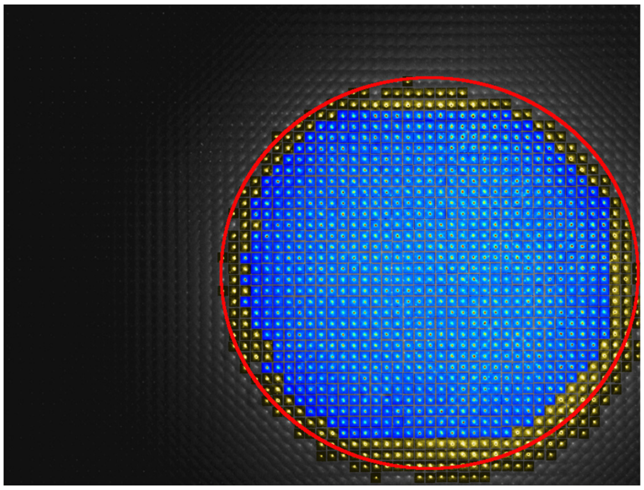

Fig. 4 Measured SH image (grayscale), detected pupil is marked red; tiles not fulfilling the quality criteria are highlighted in yellow; for calculation, selected tiles are highlighted in blue.

Scatter filters Tiffen Black Pro Mist (BPM 1/8; 1/4; 1/2; 1; 2; 3, The Tiffen Company, Hauppauge, New York) were positioned in front of the volunteer's eye during C-Quant and scatter measurements to generate straylight emulating scatter in the lens, as previously described.[3,10,26,27] The filters were arranged at an angle of 16 deg to prevent imaging the reflection of the laser beam from the surface of the filter.

2.5 *Statistical Analysis*

The statistical analysis of the data extracted from all recordings was performed using SPSS Version 19.0.0 (SPSS Inc., Chicago, Illinois). Correlations of each parameter with the filter number, C-Quant straylight parameter $\mathrm{Log}(\mathrm{IS_c})$, and each other were analyzed. Spearman's ρ rank correlation test was used under the assumption of a nonlinear correlation among the scatter parameters, filter numbers, and $\mathrm{Log}(\mathrm{IS_c})$.

3 Results

Independent of the applied stop geometry, the measurement device has a stable and triggered image acquisition with 20 frames per second. Five repeated runs for each measurement sequence lead to a total measurement time of about 6 s.

Laser safety according to DIN EN 60825-1 was proofed. With a laser power of 62.8 μW, the system is classified in laser safety class 1. The maximum permissible exposure for over 8 h is underrun by a factor of approximately 10. The laser beam diameter is approximately 0.8 mm at the cornea.

Figure 4 shows a measured SH image with a visual angle of 4 deg. The complete image is shown in grayscale. All found and separated PSFs used for the pupil detection are highlighted. The detected pupil is marked with a red ellipse. Using the minimum quality criteria, the blue highlighted tiles are selected for further calculations. Furthermore, a halo surrounding the pupil can be seen. As no subaperture PSFs are imaged in these tiles, they are not detected.

Figure 5 is showing an SH image taken with and without the scatter filter BPM1. Both images are taken with an open stop. The intensity profile of the image with BPM1 is lower than the intensity profile of the image taken without filter, because of the reduced transmittance.

Fitting Eq. (3) to the measured mean intensities $I(\theta)$ worked well with a coefficient of determination for all subjects and filters of $R^2 = 0.994$ with a standard deviation of $\mathrm{SD} = 0.0086$.

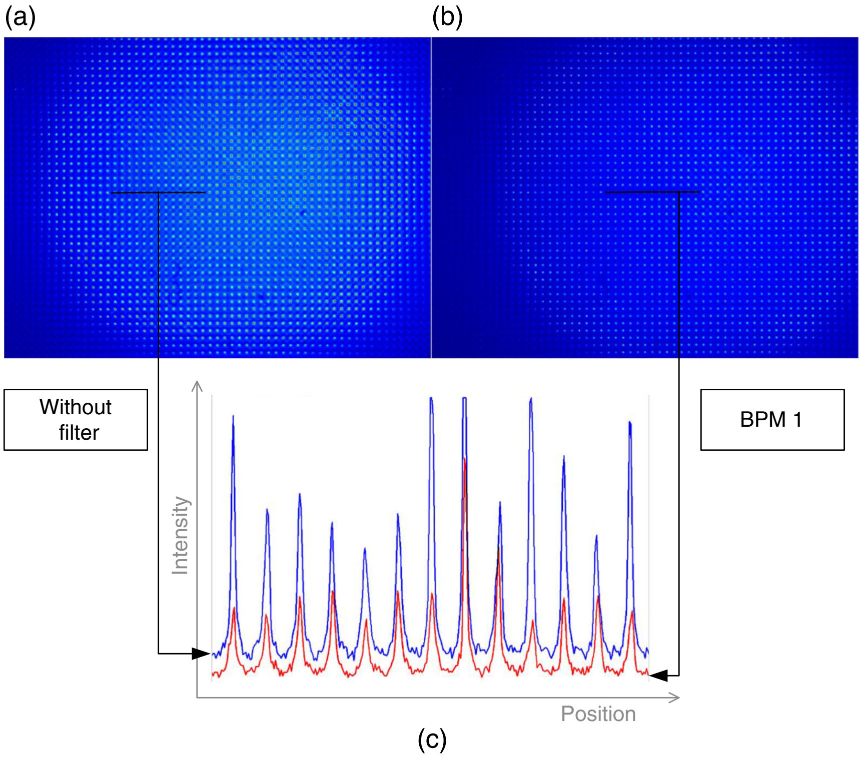

Fig. 5 Raw images (a) without filter and (b) with filter BPM 1, both with open stop. (c) The corresponding intensity profiles of the selected section indicated by the black lines are displayed (raw in blue, BPM1 in red).

Figure 6(a) shows the normalized fits of the integrals of the PSF on the fundus exemplarily for one eye with different scatter filters. Within the intensity profiles, it can be seen that the slope of the curves with less scattering are more bulged and that the curves with more scattering get flatter. Their derivations, including energy corrections, are the PSFs shown in Fig. 6(b). The slopes of the right's almost linear parts of the curves at larger visual angles get smaller with increasing scatter. Furthermore, clear differences in amplitude caused by correction of the increasing transmission loss with increasing filter density can be seen. The curves in Fig. 6(b) are clearly separated, allowing for a subsequent straylight quantification.

Correlation analysis shows a significant correlation of the C-Quant straylight parameter $\mathrm{Log}(\mathrm{IS}_c)$ with the filter values (Table 1). The scatter parameter S is significantly correlated with the filter value (see also Fig. 7[a]) as well as with $\mathrm{Log}(\mathrm{IS}_c)$. The parameter F shows significant but weaker correlation with the filter values [see Fig. 7(b)]. Scatter parameters described in our previous work and by other authors[8,13,14,16,19] show no or only weak correlations with the filter values and the C-Quant straylight parameter. The CAHM is not correlated with the filters or C-Quant, whereas it is weakly but significantly correlated with the MOM. In turn, MOM is weakly but significantly correlated with the filter values, $\mathrm{Log}(\mathrm{IS}_c)$, as well as with the scatter parameters S, F, and Log(IS). It can also be seen that S, F, and MOM are weakly correlated with the refraction, i.e., sphere and cylinder.

The one-way ANOVA shows a significant dependency ($p < 0.01$) of Log(IS) with the filter values as shown in Fig. 8. Measurements without and with filters BPM 1/8, BPM 1/4, BPM 1/2, and BPM 1 show an increase in Log(IS) as expected. BPM 3 is also increased compared to BPM 2. The noticeable gap between BPM 1 and 2 is caused by the much lower transmission of BPM 2 and 3.

Log(IS) is linearly correlated with C-Quant $\mathrm{Log}(\mathrm{IS}_c)$ (Fig. 9). The linear regression function has a slope of 0.991 and an offset of 0.784.

4 Discussion

The main objective of this work was the establishment of a measurement principle using a variable stop combined with an SH sensor and a PSF reconstruction algorithm to overcome the current limitations in objective straylight analysis.

We showed that the overlapping parts of the subaperture PSFs can be reconstructed by derivation of the PSF integral measured in a sequence of SH images with increasing field stop diameter. This stop lies in the intermediate image plane in the relay system. The resulting, rotationally symmetric PSFs span an angle of 4 deg on the fundus and can be evaluated with parameters similar to the Stiles Holladay approximation. The functionality of this method was tested by measuring the increase in scatter in the eyes of volunteers with scatter filters. Our scatter parameters S and F are highly significantly correlated with the scatter intensity of the filters and the C-Quant's straylight parameter $\mathrm{Log}(\mathrm{IS}_c)$. Furthermore, a linear dependency of the derived scatter parameter Log(IS) to the $\mathrm{Log}(\mathrm{IS}_c)$ was found.

In common wavefront aberrometers, imaging of the PSFs with subapertures of the SH sensor leads to an overlap of the images of the subaperture PSFs periphery above 1 to 2 deg visual angle. However, the central parts of the subaperture PSFs are dominated by aberrations.[27,28]

Although earlier investigations showed the ability of SH wavefront aberrometers to measure scatter within a small angle (within the subaperture),[13,14] small amounts of scatter were only measurable in eyes with low refractive error.[8] Following the assumption of van den Berg, straylight gets importance in an angular range beyond 2 deg.[27]

Furthermore, the reflection of the incoming laser beam on the background of the eye depends on the scatter properties of the fundus. Thus, the central part of the subaperture PSFs is also influenced by fundus scattering.

Owing to these facts, we increased the spatial dynamic range up to 4 deg. A direct imaging of the subaperture PSFs up to that angle with a typical optical design of a wavefront aberrometer without changing its resolution and sensitivity for aberration measurement has not been achieved so far. Therefore, we replaced the pinhole in the intermediate image plane in the relay system by a reflective display (DMD). As a consequence, we were able to vary the stop geometry in diameter. Increasing the stop diameter leads to an increase in image intensity. That functional relationship is used to reconstruct the PSF of the eye, assuming its rotational symmetry. We demonstrate that it

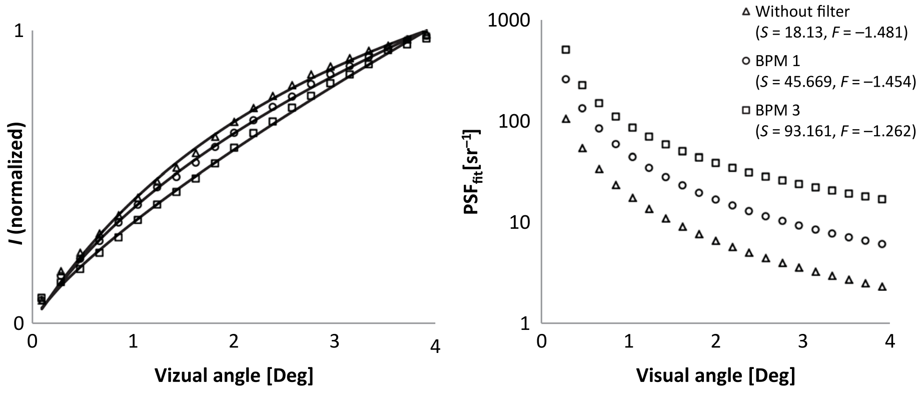

(a) (b)

Fig. 6 Normalized fit of (a) the intensity profiles and (b) PSFs of one eye under three experimental conditions: Without scatter filter (triangles), with filter BPM 1 (circles), and with filter BPM 3 (squares). (a) The markers indicate the values based on the measurements and the lines indicate the fitted curves. (b) The markers indicate the computed values according to Eq. (6).

Table 1 Correlation coefficients r and levels of significance p (Spearman–Rho correlation) among the parameters.

Parameters		Filter value	S	F	Log(IS)	C-Quant Log($\mathrm{IS_c}$)	CAHM	MOM	Sphere	Cylinder
Filter value	r	1.000	**0.861**	**−0.394**	**0.847**	**0.948**	0.041	**0.498**	0.000	0.000
	p	—	**0.000**	**0.000**	**0.000**	**0.000**	0.666	**0.000**	1.000	1.000
S	r	**0.861**	1.000	−0.199	**0.794**	**0.823**	−0.033	**0.319**	*−0.261*	0.046
	p	**0.000**	—	*0.039*	**0.000**	**0.000**	0.737	**0.001**	*0.010*	0.652
F	r	**−0.394**	*−0.199*	1.000	**−0.695**	**−0.401**	0.017	**−0.628**	*−0.208*	*−0.275*
	p	**0.000**	*0.039*	—	**0.000**	**0.000**	0.862	**0.000**	*0.041*	*0.006*
Log(IS)	r	**0.847**	**0.794**	**−0.695**	1.000	**0.816**	−0.066	**0.592**	−0.021	0.158
	p	**0.000**	**0.000**	**0.000**	—	**0.000**	0.495	**0.000**	0.837	0.121
C-Quant Log($\mathrm{IS_c}$)	r	**0.948**	**0.823**	**−0.401**	**0.816**	1.000	0.084	**0.513**	−0.002	0.019
	p	**0.000**	**0.000**	**0.000**	**0.000**	—	0.376	**0.000**	0.981	0.856
CAHM	r	0.041	−0.033	0.017	−0.066	0.084	1.000	**0.423**	−0.051	0.121
	p	0.666	0.737	0.862	0.495	0.376	—	**0.000**	0.618	0.235
MOM	r	**0.498**	**0.319**	**−0.628**	**0.592**	**0.513**	**0.423**	1.000	*0.212*	**0.325**
	p	**0.000**	**0.001**	**0.000**	**0.000**	**0.000**	**0.000**	—	*0.036*	**0.001**
Sphere	r	0.000	*−0.261*	*−0.208*	−0.021	−0.002	−0.051	*0.212*	1.000	−0.106
	p	1.000	*0.010*	*0.041*	0.837	0.981	0.618	*0.036*	—	0.301
Cylinder	r	0.000	0.046	*−0.275*	0.158	0.019	0.121	**0.325**	−0.106	1.000
	p	1.000	0.652	*0.006*	0.121	0.856	0.235	**0.001**	0.301	—

Italic: $p < 0.05$; bold: $p < 0.0014$ (Bonferroni-corrected).

is possible to measure scatter relevant parameters within the reconstructed $\mathrm{PSF_{eye,fit}}$.

The double-pass imaging of the PSF is actually not a full double-pass imaging in our case.[29] The laser beam first passes the optics of the eye with a small diameter of approximately 0.8 mm. Therefore, the first pass is not considerably influenced by aberrations.

Only the second pass uses the full pupil of the eye and is thus aberrated. Navarro et al. showed the high similarity between the PSF obtained with such an asymmetric double-pass method and the real single pass PSF.[29,30]

Compared to Artal et al.[31] and Ginis et al.,[10] our device has the advantage of measuring forward scatter objectively and the possibility of simultaneously measuring the wavefront of the

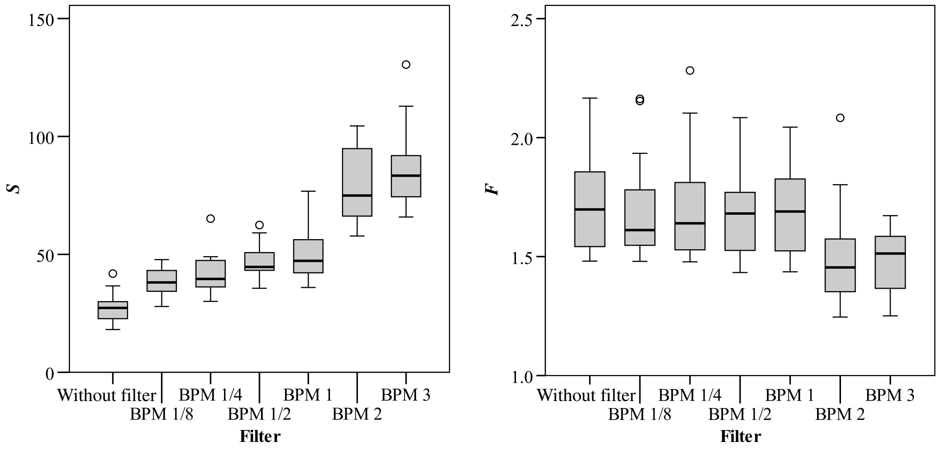

(a)

(b)

Fig. 7 Filter dependency of scatter parameters: (a) S and (b) F.

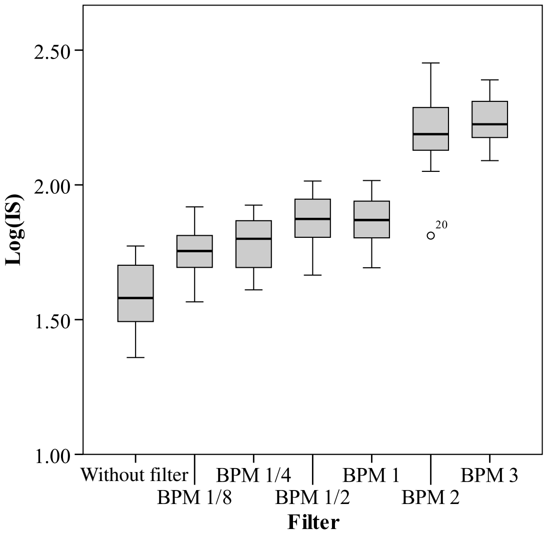

Fig. 8 Filter dependency of scatter parameter Log(IS).

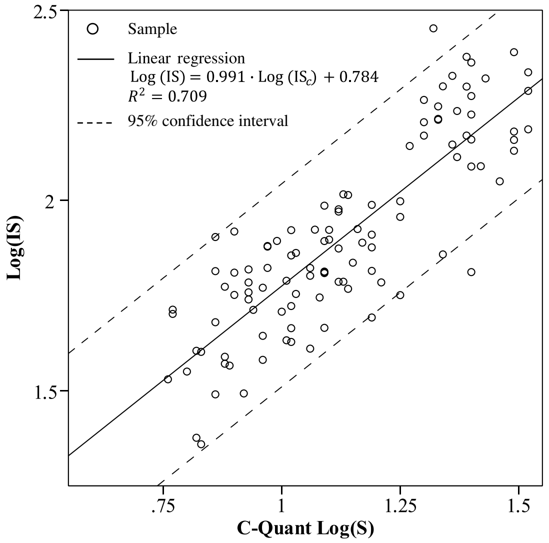

Fig. 9 Scatter plot of Log(IS) and C-Quant's straylight parameter Log(IS_c) with linear regression curve and 95% confidence interval.

eye. With a measurable field of 4 deg, we exceed the relatively small angle of the OQAS (Visiometrics S.L., Terrassa, Spain) double-pass imager.[31] However, we do not reach the measurement range of 8 deg of the device published by Ginis et al.[10] Our basic imaging system, the SH sensor, enables a local resolution of scatter sources in the pupil plane, which will be one of the next steps in our investigations. In contrast to the established C-Quant straylight meter, we do not measure the psycho-physiological response on scatter, but we can objectively quantify the intraocular scatter without volunteer or patient interaction. With a coefficient of variation of Log(IS) less than 1.5%, the repeatability is high. The pupil and the subaperture images are detected in every SH image. Therefore, eye movements do not have a considerable influence.

A limiting aspect for our device is the used wavelength of 658 nm. We do not measure the spectrum of scatter. Coppens et al.[32] measured straylight at 7 deg and showed a wavelength dependency of straylight but only with small differences between red and green light.

Ginis et al.[11] measured scatter and showed a prominent wavelength dependency of the diffusion at 1 degree, which reduces with increasing angles. Here, diffusion means the additional scatter caused within the fundus. While green light is mainly scattered in the retina and absorbed by the retinal pigment epithelium, red light penetrates deeper to the choroidea of the fundus. This leads to a widening of the reflection of the laser beam and adds a widening to the measured PSF. The diffusion process additionally depends on the pigmentation on the eye.[10,11] The variance of Log(IS) in our study is of similar size compared to measurements from literature.[11,33]

Preliminary investigations were also performed with a green laser (532 nm). However, subjects felt blinded by the green light although the laser power was much lower than the critical value and lower than the one of the red laser.

Figure 9 shows an offset of Log(IS) compared to Log(IS_C). This offset is constant in the logarithmic scale. The main reason for this offset is that the entrance beam is scattered both on the first and on the second pass. This leads to an overestimation of the forward scatter by a factor of nearly two. Although the laser beam enters the eye parallel to the optical axis to prevent reflections from the cornea, backscatter from cornea and lens are still imaged. With increasing scatter density, backscatter increases, too.[34] This is another reason for the offset in the logarithmic scale of Log(IS) and Log(IS_C). Moreover, the measurement angles of the C-Quant and our device are different. Because of the larger measurement angle of 7 deg of the C-Quant, the impact of the fundus scatter is lower. Considering our system parameters (658 nm, 4 deg visual angle), our scatter values are comparable to Ginis et al.[11] and Coppens et al.[32]

Coppens et al.[32] developed a model function for the retinal straylight, taking into account age, pigmentation, and wavelength. Using that model on our data would enable the extrapolation of our straylight parameter Log(IS) for red light to an equivalent straylight parameter for green light. Further investigations need to be conducted in this respect.

Compared to the literature, our measured PSF integrals and respective PSFs are slightly deviating to the known shape.[11,35] The main reason lies in our setup with a maximum imaging angle of 4 deg. Consequently, we normalize with respect to the intensity values found at 4 deg. In Fig. 6(a), it can be seen that the integrals still have a slope at 4 deg. That means that with a theoretically further opening of the stop, the intensity would also increase. Normalizing at a point where the PSF energy is not in saturation affects the shape of the integrals and, respectively, the PSF shape. In addition, diffraction at stops with small diameters leads to a PSF widening in a small angular region. Moreover, the above-mentioned recording of double forward scatter and backscatter might contribute to the different PSF shapes.

A further development of our measurement principle will address the increase in the measurement range beyond 4 deg. The impairment due to backscatter can be reduced by digitally separating and analyzing the entrance region of the laser beam in the pupil plane. However, our PSF also includes scatter information that is useful for assessment of the visual system. Further investigations will also address the separation of aberrations and scatter by taking into account the measured wavefront.

For a clinical use, our technique and method can be an add-on for future wavefront aberrometers, forming one of three modalities in one device, i.e., wavefront aberrometry, the previously described subaperture-based scatter measurement,[8,13–18] which works well in cataractous eyes with low effort and our wide-angle PSF reconstruction technique for low amounts of scatter. With respect to the actual high costs of the DMD, a simpler setup is envisioned, such as with a motor-driven iris diaphragm. This will enable an affordable and widely available aberrometer system for objectively measuring the main optical influences on the visual acuity, i.e., on refractive errors and scatter.

Acknowledgments

This research was supported by the German Federal Ministry of Economic Affairs (KF2250118UW4) and the German Federal Ministry of Education and Research (03IPT605X).

References

1. J. J. Vos, "Disability glare—a state of the art report," *CIE J.* **3**(2), 39–53 (1984).
2. T. J. T. P. van den Berg et al., "History of ocular straylight measurement: a review," *Z. Med. Phys.* **23**(1), 6–20 (2012).
3. G. C. de Wit et al., "Simulating the straylight effects of cataracts," *J. Cataract Refractive Surg.* **32**(2), 294–300 (2006).
4. D. P. Pinero, D. Ortiz, and J. L. Alio, "Ocular scattering," *Optom. Vision Sci.* **87**(9), E682–E696 (2010).
5. P. W. De Waard et al., "Intraocular light scattering in age-related cataracts," *Invest. Ophthalmol. Visual Sci.* **33**(3), 618–625 (1992).
6. L. Franssen, J. E. Coppens, and T. J. T. P. van den Berg, "Compensation comparison method for assessment of retinal straylight," *Invest. Ophthalmol. Visual Sci.* **47**(2), 768–776 (2006).
7. I. Guber et al., "Reproducibility of straylight measurement by C-Quant for assessment of retinal straylight using the compensation comparison method," *Graefes Arch. Clin. Exp. Ophthalmol.* **249**(9), 1367–1371 (2011).
8. S. Schramm et al., "A modified Hartmann–Shack aberrometer for measuring stray light in the anterior segment of the human eye," *Graefes Arch. Clin. Exp. Ophthalmol.* **251**(8), 1967–1977 (2013).
9. T. Bal et al., "Influence of cataract morphology on straylight and contrast sensitivity and its relevance to fitness to drive," *Ophthalmologica* **225**(2), 105–111 (2011).
10. H. Ginis et al., "The wide-angle point spread function of the human eye reconstructed by a new optical method," *J. Vis.* **12**(3), 20–20 (2012).
11. H. S. Ginis et al., "Wavelength dependence of the ocular straylight," *Invest. Ophthalmol. Visual Sci.* **54**(5), 3702–3708 (2013).
12. L. N. Thibos et al., "Standards for reporting the optical aberrations of eyes," *J. Refractive Surg.* **18**(5), 652–660 (2002).
13. W. J. Donnelly, III et al., "Quantifying scatter in Shack–Hartmann images to evaluate nuclear cataract," *J. Refractive Surg.* **20**(5), S515–S522 (2004).
14. W. J. Donnelly, III, "Measuring and modeling intraocular light scatter with Shack–Hartmann wavefront sensing and the effects of nuclear cataract on the measurement of wavefront error," Dissertation, University of Houston (2005).
15. R. A. Applegate and L. N. Thibos, "Methods and systems for measuring local scattering and aberration properties of optical media," U.S. Patent No. 6,905,210 B2 , p. 21 (2005).
16. T. Fujikado et al., "Light scattering and optical aberrations as objective parameters to predict visual deterioration in eyes with cataracts," *J. Cataract Refractive Surg.* **30**(6), 1198–1208 (2004).
17. T. Mihashi et al., "Intensity analysis of Hartmann-Shack images in cataractous, keratoconic, and normal eyes to investigate light scattering," *Jpn. J. Ophthalmol.* **50**(4), 323–333 (2006).
18. A. Cervino et al., "Objective measurement of intraocular forward light scatter using Hartmann–Shack spot patterns from clinical aberrometers: model-eye and human-eye study," *J. Cataract Refractive Surg.* **34**(7), 1089–1095 (2008).
19. T. Kuroda et al., "Effect of aging on ocular light scatter and higher order aberrations," *J. Refractive Surg.* **18**(5), S598–S602 (2002).
20. T. J. van den Berg, "To the editor: intra-and intersession repeatability of a double-pass instrument," *Optom. Vision Sci.* **87**(11), 920–921 (2010).
21. R. E. Dorsey and W. J. Mayer, "Genetic algorithms for estimation problems with multiple optima, nondifferentiability, and other irregular features," *J. Bus. Econ. Stat.* **13**(1), 53–66 (1995).
22. M. B. Gordy, "Genetic algorithms toolbox for Matlab," (1996), http://www.geatbx.com/links/genetic_maximization_matlab_m_gordy.html (2 May, 2012).
23. J. J. Vos, "Reflections on glare," *Light. Res. Technol.* **35**(2), 163–176 (2003).
24. J. J. Vos, "On the cause of disability glare and its dependence on glare angle, age and ocular pigmentation," *Clin. Exp. Optom.* **86**(6), 363–370 (2003).
25. T. J. T. P. van den Berg, "Analysis of intraocular straylight, especially in relation to age," *Optom. Vision Sci.* **72**(2), 52–59 (1995).
26. P. H. B. Kok et al., "A model for the effect of disturbances in the optical media on the OCT image quality," *Invest. Ophthalmol. Visual Sci.* **50**(2), 787–792 (2009).
27. T. J. T. P. van den Berg, L. Franssen, and J. E. Coppens, "Straylight in the human eye: testing objectivity and optical character of the psychophysical measurement," *Ophthalmic Physiol. Opt.* **29**(3), 345–350 (2009).
28. N. López-Gil and P. Artal, "Comparison of double-pass estimates of the retinal-image quality obtained with green and near-infrared light," *J. Opt. Soc. Am. A* **14**(5), 961–971 (1997).
29. R. Navarro and M. Losada, "Phase transfer and point-spread function of the human eye determined by a new asymmetric double-pass method," *J. Opt. Soc. Am. A* **12**(11), 2385–2392 (1995).
30. P. Artal et al., "Double-pass measurements of the retinal-image quality with unequal entrance and exit pupil sizes and the reversibility of the eye's optical system," *J. Opt. Soc. Am. A* **12**(10), 2358–2366 (1995).
31. P. Artal et al., "An objective scatter index based on double-pass retinal images of a point source to classify cataracts," *PLoS One* **6**(2), e16823 (2011).
32. J. E. Coppens, L. Franssen, and T. J. T. P. van den Berg, "Wavelength dependence of intra ocular straylight," *Exp. Eye Res.* **82**, 688-692 (2006).
33. H. Ginis et al., "Compact optical integration instrument to measure intraocular straylight," *Biomed. Opt. Express* **5**(9), 3036 (2014).
34. D. R. Williams et al., "Double-pass and interferometric measures of the optical quality of the eye," *J. Opt. Soc. Am. A* **11**(12), 3123–3135 (1994).
35. J. J. Vos, J. Walraven, and A. Van Meeteren, "Light profiles of the foveal image of a point source," *Vision Res.* **16**(2), 215–219 (1976).

Stefan Schramm received his MS degree in mechanical engineering in the field of quality management from Ilmenau University of Technology in 2007. He is a scientific assistant at the Institute of Biomedical Engineering and Informatics, Ilmenau University of Technology. Currently, he is working on a doctorate in biomedical engineering with specialization in ophthalmological diagnostics. He is the author of two peer-reviewed journal papers. His research interests include scatter measurement, numerical optical modeling, and optoelectronic systems.

Jens Haueisen received his PhD in electrical engineering from the Technical University Ilmenau, Germany, in 1996. From 1996 to 1998, he worked as a postdoc, and from 1998 to 2005, as the head of the Biomagnetic Center, Friedrich-Schiller-University, Jena, Germany. Since 2005, he directs the Institute of Biomedical Engineering and Informatics at the Technical University Ilmenau, Germany. His research interests include the investigation of bioelectric and biomagnetic phenomena and medical technology for ophthalmology.

Daniel Baumgarten received his master's and PhD degrees in biomedical engineering from TU Ilmenau, Germany, in 2006 and 2011, respectively. Since 2013, he has been an assistant professor for multimodal data analysis in biomedical engineering at TU Ilmenau. In 2016, he was appointed a full professor for electrical and biomedical engineering at UMIT, Hall in Tirol, Austria. His research interests include ophthalmic medical technology, bioelectromagnetic modeling and source reconstruction, and medical imaging, and image processing.

Biographies for the other authors are not available.